Soft Matter

Accepted Manuscript

This article can be cited before page numbers have been issued, to do this please use: F. Wang, Z. Wang, Y. Peng, Z. Zheng and Y. Han, *Soft Matter*, 2018, DOI: 10.1039/C7SM02291C.

ROYAL SOCIETY OF CHEMISTRY

rsc.li/soft-matter-journal

View Article Online
DOI: 10.1039/C7SM02291C

Soft Matter

ARTICLE TYPE

Cite this: DOI: 10.1039/xxxxxxxxxx

Homogeneous melting near the superheat limit of hard-sphere crystals†

Feng Wang,[a] Ziren Wang,[b] Yi Peng,[a] Zhongyu Zheng,[c,d] and Yilong Han*[a]

Received Date
Accepted Date

DOI: 10.1039/xxxxxxxxxx

www.rsc.org/journalname

A defect-free crystal can be superheated into a metastable state above its melting point and eventually melts via homogeneous nucleation. Further increasing the temperature leads to the metastable crystal becoming unstable and melting catastrophically once beyond its superheat limit. The homogeneous melting is not well studied near the superheat limit and this limit is difficult to measure accurately, even for the simplest model of hard-sphere crystals. Here our molecular-dynamics simulations identify its superheat limit at volume fraction $\phi_{\rm limit} = 0.494 \pm 0.003$, which is higher than the previous theoretical estimations. We found that the hard-sphere crystal at the superheat limit does not satisfy Born's melting criterion, but has a vanishing bulk modulus, i.e. a spinodal instability, which preempts other thermodynamic or mechanical instabilities. At the strong superheating regime, the nucleation deviates from the assumptions in the classical nucleation theory. In contrast to crystallization which often develops nuclei with various intermediate structures, the melting of face-centered cubic (fcc) hard-sphere crystal does not produce intermediate structures such as body-centered cubic (bcc) crystallites although bcc is more stable than fcc at the strong superheating regime. Moreover, we found that the time evolutions of the order parameters and the pressure all exhibit a compressed exponential function, in contrast to the stretched exponential relaxation of supercooled liquids. The compressed exponential functions have the same exponent, which poses a new challenge to theory.

1 Introduction

Crystal melting is a well-known first-order phase transition which lacks a fundamental theory[1–3]. It is connected to other areas of physics such as insulator-conductor transition through melting of the Wigner crystal formed by electrons[4], glass transitions[5,6] and superstring theory[7], as well as other disciplines such as biology and environmental science. Melting usually begins heterogeneously from free surfaces[1,8] or grain boundaries[9] when crystals are heated to the melting point. By suppressing the melting from surfaces, a crystal can be superheated above its melting point. Such a superheated metastable crystal is rare in nature, but can be experimentally achieved by the following two methods: (1) Coating a single crystal with a high-melting-point material[10,11]. The possible interface and edge melting can be avoided when the solid-solid interfaces have a high enough affinity. (2) Heating the interior of a crystalline domain with a focused beam of light[12–15]. The metastable state of the superheated crystal and the liquid nucleation during the melting have been experimentally achieved under a quasistatic light heating[14]. The melting of superheated crystals has broad implications in technologies such as laser-processing materials[16] and explosive materials[17]. When the degree of superheating is increased beyond a threshold value, the crystal becomes unstable and melts catastrophically from everywhere rather than via nucleation, due to the vanishing of the free-energy barrier between crystal and liquid phases. This superheat limit sets the condition for the existence of crystals[2]. In contrast to the intensively studied supercool limit of liquids (i.e. the glass transition point), the superheat limit of crystals has been much less studied.

Homogeneous melting of surface- and defect-free crystals is of fundamental interest. For two-dimensional (2D) melting, both the KTHNY theory[18] and the grain-boundary-mediated melting theory[19] only apply to infinitely large, defect- and surface-free 2D crystals. They have been intensively studied and tested by experiments[20,21] and simulations[22–24]. Three dimensional (3D) homogeneous melting of superheated crystals has been studied in theories[25–27], simulations[28–31] and experiments[10–14], but it remains

[a] Department of Physics, the Hong Kong University of Science and Technology, Clear Water Bay, Hong Kong, China. E-mail: yilong@ust.hk
[b] Department of Physics, Chongqing University, Chongqing 401331, China.
[c] Institute of Mechanics, Chinese Academy of Sciences, Beijing 100190, P.R.China.
[d] University of Chinese Academy of Sciences, No.19(A) Yuquan Road, Shijingshan District, Beijing, 100049, P.R.China.

† Electronic Supplementary Information (ESI) available: calculation of pressure and elastic moduli, estimation of critical nucleus size by the classical nucleation theory. See DOI: 10.1039/cXsm00000x/

View Article Online
DOI: 10.1039/C7SM02291C

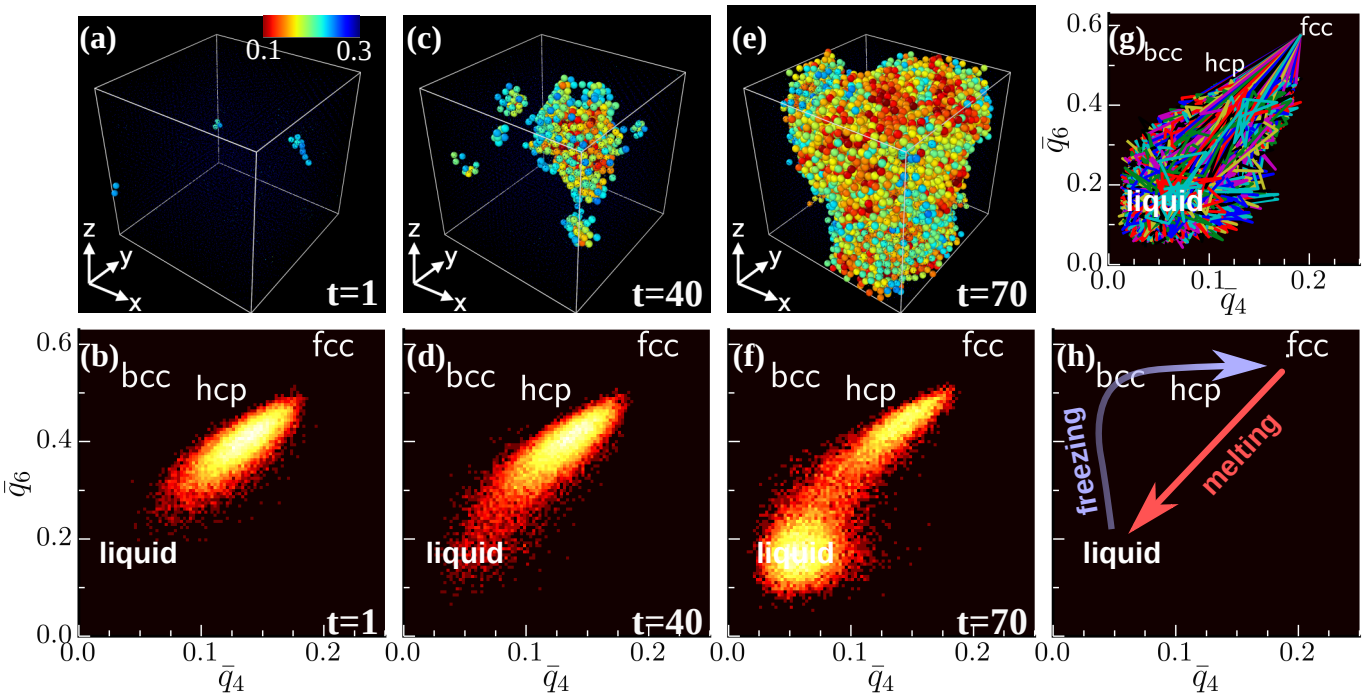

Fig. 1 Melting kinetics of a superheated crystal at $\phi = 0.50$ containing 4×16^3 particles. (a, c, e) Real-space configurations of liquid-like particles colored according to their $\bar{q}_6$ (Movie 1). The colorbar of $\bar{q}_6$ is in (a). Crystalline particles are not shown. (b, d, f) $\bar{q}_6$ and $\bar{q}_4$ of all particles corresponding to (a, c, e) respectively (Movie 2). The intensity of the color represents the logarithm of statistical counts. The "bcc", "hcp", and "fcc" labels denote the locations of these perfect crystals at zero temperature. Thermal noises make the distribution in (b) deviate from the perfect fcc lattice. Note that the largest nucleus in (c) is already post-critical. (g) Trajectories of all particles in the $\bar{q}_6$-$\bar{q}_4$ plane. (h) Schematic of the melting and freezing kinetics.

challenging to accurately measure the melting behaviors near the superheat limit. The superheated hard-sphere crystal melting has only been briefly studied in simulation without exploring the nucleation and the superheat limit[32]. The hard-sphere system is the simplest model exhibiting melting and freezing transitions. This system is particularly useful for understanding crystal-liquid phase transitions because these transitions depend primarily on the hard cores of atoms[33]. The system is a good model for the commonly used colloids[34] and serves as a reference system for the perturbation theories of real materials[35]. The phase diagram of hard spheres in 3D has been well established (Fig. S1 in Electronic Supplementary Information (ESI))[35] but the superheat limit has not. The superheat limit of hard-sphere crystals has been estimated using different theories including the single-occupancy model[36] and density functional theory (DFT) with various approximations[35,37–40]. Whereas hard-sphere crystallization has been studied intensively both experimentally and via simulation, the melting of hard-sphere crystals has rarely been simulated under strong superheating. Experimentally, the melting of superheated crystals has been observed at the single-particle level in colloidal systems, but the kinetics are too rapid to measure under strong superheating; moreover, colloidal spheres are not exactly hard spheres[14,41]. Hence the superheat limit of hard-sphere crystals remains unknown and the melting kinetics around the limit are unclear.

Here, we address these questions and identify the superheat limit of the hard-sphere crystal at volume fraction $\phi_{\text{limit}} = 0.494 \pm 0.003$ by three methods consistently: (1) the vanishing of metastable crystal through the time evolutions of the order parameters, (2) the vanishing of an elastic modulus, and (3) the finite-size effect on the nucleation processes. We show that the superheat limit is set by the vanishing of the bulk modulus, preempting the conventional Born's shear instability.

2 Methods

We performed event-driven molecular dynamics simulations of the hard-sphere system with mass $m = 1$, diameter $\sigma = 1$ and thermal energy $k_B T = 1$. The time unit $\tau_0 = \sqrt{m\sigma^2/k_B T}$ is the amount of time a sphere usually takes to travel the distance of one diameter. The unit cell of the face-centered cubic (fcc) lattice is cubic and contains four particles. The whole simulated crystal is cubic and contains L^3 cubic unit cells. To measure the finite-size effect, $N = 4L^3$ ($L = 4,\ 8,\ 16,\ 32,\ 64$) spheres were initially placed at the perfect fcc lattice sites and assigned random initial velocities following the Maxwell-Boltzmann distribution. Periodic boundary conditions are used to avoid surface melting. The volume fraction ϕ is defined as the fraction of volumes occupied by the spheres. A lower ϕ corresponds to a higher temperature in an atomic system. The hard-sphere fcc crystal has the melting point $\phi_m = 0.545$, and a crystal becomes superheated and metastable at $\phi < \phi_m$.

We monitored the structural evolution using the global translational order parameter Q_T, the global orientational order parameter $Q_{4,6}$, and the local orientation order parameters $\bar{q}_{4,6}$

View Article Online
DOI: 10.1039/C7SM02291C

which reflect different crystalline symmetries. The global translational order parameter $Q_{\mathrm{T}} = \frac{1}{N}\sum_i \cos \mathbf{k}\cdot\mathbf{r}_i$, the global orientational order parameter $Q_l = \sqrt{\frac{4\pi}{2l+1}\sum_{m=-l}^{l}\left|\frac{1}{N}\sum_i q_{lm}(i)\right|^2}$, and the local orientational order $q_l(i) = \sqrt{\frac{4\pi}{2l+1}\sum_{m=-l}^{l}|q_{lm}(i)|^2}$, where $q_{lm}(i) = \frac{1}{N_{\mathrm{b}}(i)}\sum_{j=1}^{N_{\mathrm{b}}(i)} Y_{lm}(\hat{\mathbf{r}}_{ij})$[42]. The wave vector $\mathbf{k}$ was measured from the position of the first peak of the structure factor $S(\mathbf{k})$. $\mathbf{r}_i$ is the position of particle i. $N_{\mathrm{b}}(i)$ is the set of nearest neighbors of particle i. Y_{lm} is the spherical harmonic function, where $l = 4$ or 6 for the symmetries of the fcc structure. Here neighboring particles are defined as those within a distance of 1.4σ of each other[43]. Moreover, we monitored the local order parameters coarse-grained over the first-shell neighbors $\bar{q}_l(i) = \sqrt{\frac{4\pi}{2l+1}\sum_{m=-l}^{l}\left|\frac{1}{N_{\mathrm{b}}(i)+1}\sum_j q_{lm}(j)\right|^2}$, where the summation index j includes all neighbors of particle i as well as i itself. $\bar{q}_{l=4,6}(i)$ contains information about the second layer of neighbors, and hence it improves the accuracy in distinguishing one local symmetry from another[44].

3 Results and Discussion

3.1 Homogeneous nucleation of liquid phase

The kinetics are important for a first-order phase transition, but they are usually difficult to predict, especially at strong supersaturation where the assumptions in classical nucleation theory (CNT) are often violated[3]. We found that the melting of the superheated defect-free crystal follows a homogeneous nucleation of liquid phase, e.g. Figs. 1a, c, e and Movie 1. Under the strong superheating ($\phi = 0.50$), deviations from the CNT assumptions are observed, such as the non-spherically-shaped nuclei and nuclei coalescence. Using CNT, we estimated the critical nucleus radius about 5σ at $\phi = 0.50$ and the free energy barrier about $80k_{\mathrm{B}}T$ based on the chemical potential difference and interfacial energy between the hard-sphere crystal and the liquid in literature[35](see section V of ESI for the calculations). Such a high barrier implies that the nucleation can never occur in a practical time scale, which contradicts to our observation (Fig. 1c). This is because the estimated value from CNT is inaccurate due to the violation of assumptions of CNT at strong superheating, including non-spherical nucleus shape with rough surfaces, curvature effects to the surface tension for tiny nuclei, and coalescence of small nuclei. It is well known that CNT works well at weak supersaturation and often breaks down at strong superstatuaration. In addition, we use the mean first passage time of liquid nucleus sizes to estimate the critical nucleus radius to be about 2.6σ (see section VI of ESI for the details), which is smaller than 5σ estimated from the CNT (see ESI) and smaller than the system size (e.g. $L = 16\sigma$). Hence the finite-size effect is small, as confirmed in section II of ESI.

When a liquid crystallizes into an fcc crystal, the nucleus often experiences an intermediate state such as a body-centered cubic (bcc) or random hexagonal close-packed (rhcp) crystallite in hard-sphere systems[45–47] because the free energy of a crystalline nucleus depends on various factors such as surface tension and crystallinity[48]. $\bar{q}_6$ and $\bar{q}_4$ of each particle averaged over two layers of neighbors are effective to distinguish different crystal structures[49]. Our measured $\bar{q}_6$ and $\bar{q}_4$ in Fig. 1b, d, f and Movie 2 show that the fcc crystal transforms directly into a liquid without any intermediate state at strong superheating, even when bcc structure is more stable than fcc structure for hard spheres at $\phi < 0.503$[50]. This single-step melting was also observed in the simulations of the superheated copper and aluminum[31] and is distinct from the multi-step pathways typically observed in crystallization[46,49], as schematically shown in Fig. 1h. These results clearly show that the kinetics of a first-order phase transition could be very different from the kinetics of its reverse transition.

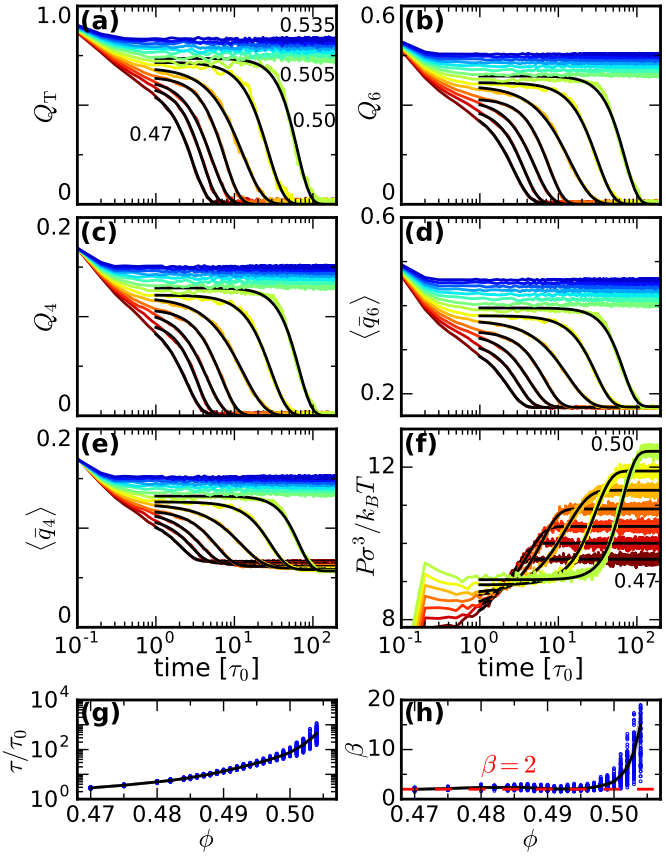

Fig. 2 Evolution of the order parameters (a) Q_{T}, (b) Q_6, (c) Q_4, (d) $\langle\bar{q}_6\rangle$, (e) $\langle\bar{q}_4\rangle$ and (f) pressure P during the melting process of a crystal containing 4×16^3 particles. 0.47 (red)$\leq\phi\leq$ 0.535 (blue) with step size 0.005. $Q_{T,6,4}$ are of order one for crystals and zero for liquids. Black curves in (a-f) are the fittings of Eq. 1. (a-f) only show a short time interval $[0, 200\tau_0]$ from the full $10^4\tau_0$ simulation. (g, h) All order parameters and pressure in (a-f) yield the same fitted melting time τ and exponent β (Fig. S2). τ and β (symbols) in the compressed exponential fits of $Q_{\mathrm{T}}(t)$ from 100 independent simulations at each ϕ. Black curves represent the average values. The red dashed line represents $\beta = 2$. Errors of τ and β are smaller than the symbol size.

3.2 The universal compressed exponential evolution of the order parameters

The evolution of order parameters and pressure exhibits plateaus at $\phi \geq 0.495$ (Figs. 2a-f), reflecting a metastable crystal. No such plateaus are observed for $\phi \leq 0.49$, indicating that the superheat limit lies within the range $0.49 < \phi_{\mathrm{limit}} < 0.495$. Interestingly, we

View Article Online
DOI: 10.1039/C7SM02291C

found that the changes of the order parameters Q_T, $Q_{6,4}$, $\bar{q}_{6,4}$ and the pressure P during melting can all be well fitted by the same functional form (Figs. 2a-f),

$$Q(t) = (Q_{\rm fcc} - Q_{\rm liquid})e^{-(t/\tau)^\beta} + Q_{\rm liquid}. \quad (1)$$

Note that the initial state is set as a perfect fcc lattice, which rapidly thermalizes to a metastable crystal during $1\tau_0$ (Fig. 2); Consequently this initial relaxation is excluded from the fitting because the fitting only describes the homogeneous melting process from a metastable crystal to a liquid. For each ϕ, different order parameters have different fitted $Q_{\rm fcc}$'s and $Q_{\rm liquid}$'s but almost the same relaxation time τ and exponent β (Fig. S2). This indicates that the homogeneous melting is a simple process that can be described by a single reaction coordinate such as Q_T. Consequently, the translational and orientational symmetries change simultaneously during melting. This is different from the typical 2D crystal melting in which the translational symmetry changes before the orientational symmetry[20].

The fitted $\beta \approx 2$ (i.e. it is Gaussian) at $\phi < 0.495$, and β increases rapidly at $\phi > 0.495$ (Fig. 2h). Eq. 1 with $\beta > 1$ is a compressed exponential function, in contrast to the commonly observed stretched exponential function with $\beta < 1$ in the relaxation of disordered systems (e.g. supercooled liquids). Stretched exponential behaviors have been intensively studied, but whether they have a universal microscopic origin remains unclear[51]. On the other hand, compressed exponential behaviors are rare and much less understood than stretched exponential behaviors. They certainly have not been reported in previous crystal-melting studies. Compressed exponential behaviors have been found in the Johnson-Mehl-Avrami-Kolmogorov (JMAK) law for nucleation processes[52], the crystallization of certain metallic glasses[53], certain types of relaxation near jamming or glass transitions[54–58], and the hyper-diffusive dynamics of nanoparticles in a supercooled solvent[59]. These examples usually have $\beta < 2$ (except the JMAK law that $\beta = 3$ or 4), indicating that the nucleation at $\phi > 0.495$ with a much higher β may have a different microscopic origin.

3.3 Spinodal instability at the superheat limit

Various possible thermodynamic instabilities may set the superheat limit of a crystal. Empirically, several stability limits have been proposed, such as the isochoric (equal volume for equilibrium liquid and superheated solid) point, the isenthalpic (equal enthalpy) point and the isentropic (equal entropy) point[2,25–27]. Isochoric instability is based on the assumption that a crystal is denser than a liquid. Isentropic instability arises when the entropy of a superheated crystal begins to exceed that of a liquid[27], analogous to the Kauzmann paradox for glass transitions. For hard-sphere crystals, the isochoric point lies at $\phi_f = 0.494$, and the isenthalpic and isentropic points lie at the same point $\phi \approx 0.515$[38] (0.517[50]). Another class of thermodynamic stability criteria initially proposed by Born is based on mechanical instabilities when one of the elastic moduli becomes zero. A 3D crystal with cubic symmetry has three independent moduli, and hence it has three types of mechanical instabilities[60]: (1) spinodal instability when the bulk modulus $B = 0$, causing the decohesion of crystal and strong density fluctuation; (2) Born instability when the shear modulus $C' = 0$, under which the symmetry is broken with the coupling of shear modes under volume conservation; and (3) the instability when another shear modulus $C_{44} = 0$. Born proposed that C' was the first to vanish among the three moduli and associated it with the melting point rather than the superheat limit. In fact, all elastic moduli are finite at the melting point so that the crystal does not melting catastrophically, but via nucleation or surface melting. Later studies showed that other elastic instabilities are possible at the superheat limit[60]. The instability of hard-sphere crystals has been theoretically studied mainly using DFT with various approximations, but the predicted instability points vary considerably as summarized in Fig. 3a and the type of instability cannot be determined. Recently, a numerical study estimated the instability point $\phi \approx 0.45$ by applying the nested sampling method to 128 spheres without determining the type of instability[61].

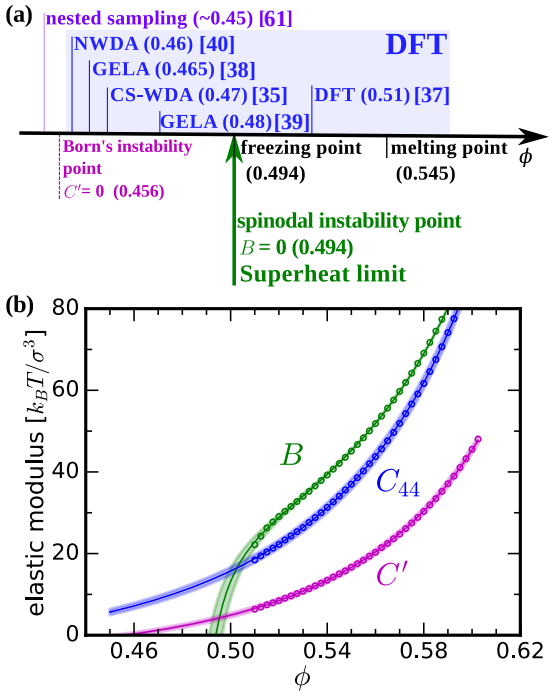

Fig. 3 Instabilities of the hard-sphere fcc crystal. (a) Values of the crystal instability point predicted theoretically and via simulation are labeled above the ϕ-axis. The spinodal point ($B = 0$, superheat limit) and Born's instability point ($C' = 0$) obtained from (b) are labeled below the axis. (b) The three measured elastic moduli fitted by Eqs. 2 and 3 (curves) show that the spinodal instability ($B = 0$) preempts the other two instabilities, setting the superheat limit at $\phi_{\rm limit} = 0.494 \pm 0.003$. The shadows around the curves represent the uncertainties in the fitting and extrapolation. Errors of the measured elastic moduli are smaller than the symbol size.

We measured B, C' and C_{44} ranging from $\phi = 0.51$ to 0.6025 using the stress-strain relation[62] (Figs. 3b and S9). A strongly superheated crystal at $\phi < 0.51$ melts too quickly for measuring the elastic moduli. Hence extrapolation is necessary to locate the mechanical instabilities. This problem exists in all studies of the superheat limits of crystals[63], and the studies of spinodal point of liquid-gas transition[52]. Conventional polynomial extrapolations

View Article Online
DOI: 10.1039/C7SM02291C

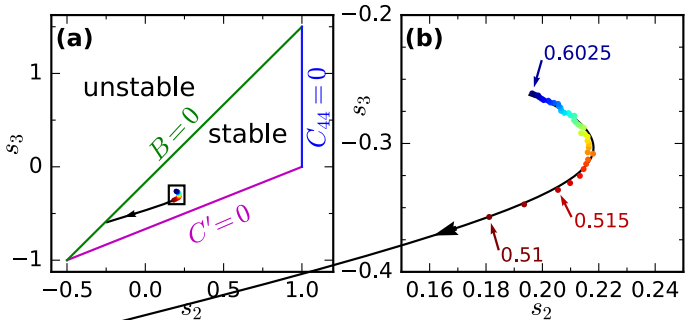

Fig. 4 (a) Elastic modulus parameters of the crystals in the stability triangle. (b) A zoom-in plot of the small rectangle in (a). The curve is calculated from the fitted B, C' and C_{44} using Eqs. 2 and 3. The arrow points to the direction that ϕ decreases. Errors of s_2 and s_3 are smaller than the size of the dot symbols.

lack physical meaning and may not correctly capture the high-density divergence of the elastic modulus or the trend near the superheat limit (see ESI). Here we use the precise equation of state (EOS) which has physical meanings and can accurately determine the superheat limit. In our fitting formula $B=\phi\frac{dP}{d\phi}$, $P(\phi)$ is given by Speedy's EOS for hard-sphere crystals[64]:

$$\frac{\pi}{6}\frac{P\sigma^3}{\phi k_B T}=-\frac{c_4}{\phi/\phi_{cp}-1}-c_1\frac{\phi/\phi_{cp}-c_2}{\phi/\phi_{cp}-c_3}. \quad (2)$$

Similarly, we propose that all elastic moduli have the same functional form

$$C=\phi\frac{df(\phi,c_1,c_2,c_3,c_4)}{d\phi}, \quad (3)$$

where the stress-like functional $f(\phi,c_1,c_2,c_3,c_4)$ takes the same form as Speedy's EOS $P(\phi)$, but the constants c_i are different for B, C' and C_{44}. Physically, the first term in Eq. 2 is derived from the free volume theory[35,64]. c_4 is related to the asymptotic divergence at the closest-packing ϕ_{cp}, $C\sim\frac{6k_BT}{\pi\sigma^3}\frac{c_4\phi/\phi_{cp}}{(\phi/\phi_{cp}-1)^2}$, and has been measured by fitting the elastic moduli data near ϕ_{cp}[65]. The second term in Eq. 2 represents the correction in the low-density regime, and has not been previously used in fitting the elastic moduli in the whole density regime. Eqs. 2 and 3 fit all of the measured elastic moduli (Fig. 3b) and yield $c_4=3.001\pm0.002,\ 2.550\pm0.001,\ 4.150\pm0.001$ for B, C', C_{44} respectively, close to the values of 3, 2.55, 4.14 measured in ref.[65]. This lends confidence to the reliability of the fitting. As a byproduct, we obtained more accurate coefficients in Speedy's EOS by fitting B for strongly superheated crystals (see section IV of ESI).

The three moduli extrapolated to zero in Fig. 3b show that the spinodal instability ($B=0$) at $\phi_{limit}=0.494\pm0.003$ preempts other instabilities, which agrees well with the observed instability at $0.49<\phi<0.495$ in Fig. 2. Interestingly this ϕ_{limit} coincides with the freezing point $\phi_f=0.494$, which is also the isochoric point for hard spheres. Although different simulations such as Monte Carlo or Brownian dynamics simulations may affect the kinetics[32], they are not expected to affect the elastic moduli and thus should yield the same superheat limit. The superheat limit is much higher than the predictions of DFT as shown in Fig. 3a[35,38–40]. Although many crystals such as the Lennard-Jones system exhibits Born's instability at the superheat limit[28], the non-Born spinodal instability at the superheat limit has also been observed in some metals, such as Au[63].

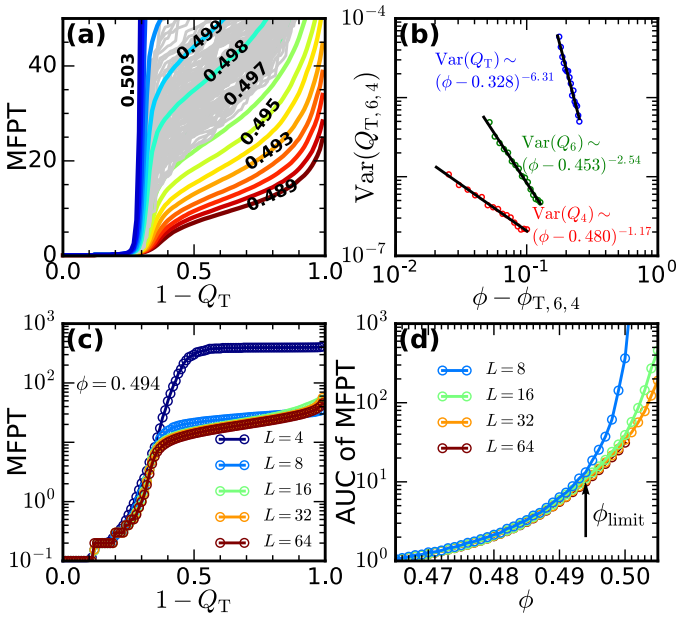

Fig. 5 (a) Mean first-passage time (MFPT) of $(1-Q_T)$ for the crystal at different ϕ's labeled on the curves. The curve at each ϕ is the average of 100 independent runs, e.g. the curve labeled with 0.498 is the average of the 100 gray curves. (b) Variance (proportional to the susceptibility[66]) of the global order parameters Q_T, Q_6 and Q_4. The power-law fittings (black lines) show that the susceptibilities of the global order parameters do not diverge at $\phi_{limit}=0.494$. (c) The MFPT of $(1-Q_T)$ of crystals of size $L=4,8,16,32,64$ at $\phi=0.494$. (d) The area under the curve (AUC) of the MFPT for various ϕ and L.

$C'=0$ preempted by $B=0$ is confirmed by the stability triangle shown in Fig. 4. We plot the elastic moduli data via two dimensionless parameters[60]

$$s_2=\frac{C_{11}-C_{44}}{C_{11}+2C_{44}},$$
$$s_3=\frac{C_{11}-C_{12}-2C_{44}}{C_{11}+2C_{44}}, \quad (4)$$

where $C_{11}=(3B+4C')/2$ and $C_{12}=(3B-2C')/3$. The elastic stability requirements $B>0$, $C'>0$ and $C_{44}>0$ form a triangle on the s_2-s_3 plane[60]. Our measured (s_2, s_3) are within the triangle, indicating that the crystals are mechanically stable. The extrapolation from the trend of measured data in Fig. 4 shows that the curve reaches the $B=0$ boundary instead of the $C'=0$ boundary. This confirms that the spinodal instability $B=0$ preempts $C'=0$ at the superheat limit. The instability triangle in Fig. 4 can identify the instability type more accurately, which has been used in determining the stability of perfect crystal structures[60] but not for superheat limit studies.

View Article Online
DOI: 10.1039/C7SM02291C

3.4 The crossover from nucleation to catastrophic melting near the superheat limit

Around the superheat limit $\phi_{\text{limit}} = 0.494$, homogeneous melting changes from a nucleation process to catastrophic melting. This change occurs gradually as demonstrated by the continuous change in the mean first-passage time (MFPT) of the disorder parameter $(1-Q_{\text{T}})$ in Fig. 5a. The MFPT measures the average first time that the system reaches a disorder parameter $(1-Q_{\text{T}})$ greater than a given value, and the average is performed over 100 independent simulation runs. Other order parameters have similar MFPTs. Furthermore, the variances of the global order parameters Q_{T}, Q_6 and Q_4 of the metastable crystals exhibit power laws (Fig. 5b), however, the extrapolated singularities cannot be reached due to the non-existence of crystal at $\phi < \phi_{\text{limit}}$, i.e. no singularity is encountered as ϕ approaches ϕ_{limit}. Hence the superheat limit is not a pseudo-spinodal point which exhibits singular behavior similar to a critical point[52].

3.5 Superheat limit identified from the finite-size effect

Our simulation shows three stages: relaxation, nucleation and post-critical nucleus growth. Particles are initially placed on the perfect lattice sites and rapidly relax to a superheated crystal with random thermal motions. This short relaxation period is independent of system size. In the second stage, the time required for generating a liquid nucleus, i.e. the incubation time, is inversely proportional to the system size $N = 4L^3$ because nuclei are equally likely to form in the system. Hence, the collapse of MFPTs to a single curve for different L's implies that the process is a relaxation of the initially perfect crystal, rather than size-dependent nucleation and growth. In other words, the end of the collapse indicates the superheat limit. Here we compare the MFPT of $(1-Q_{\text{T}})$ at a fixed ϕ (Fig. 5c) and the area under the curve of the MFPT at various ϕ (Fig. 5d) for various system size up to $L = 64$ (i.e. ~ 1.05 million particles). The end of collapse is observed at $\phi_{\text{limit}} = 0.494$, as labeled in Fig. 5d, which confirms the result obtained by elastic modulus. The collapse of the MFPTs of $L = 8$ to 64 (Fig. 5c) also indicates a negligible finite-size effect. The longer MFPT (i.e. the higher stability of the crystal) for $L = 4$ is likely attributed to the suppression of long-wave-length fluctuations in such a small system.

3.6 Lindemann melting criterion

The Lindemann parameter $\tilde{L} = \sqrt{\langle \Delta r^2 \rangle}/a$ measures the mean vibrational amplitude of particles, where Δr is the distance to the equilibrium position (i.e. the lattice site) and a is the lattice constant. Many materials have similar $\tilde{L}$ at the melting point and thus the value of $\tilde{L}$ is used as an empirical melting criterion. Our measured Lindemann parameter $\tilde{L}(\phi_{\text{m}}) = 0.124$ at the melting point and $\tilde{L}(\phi_{\text{limit}}) = 0.193$ at the superheat limit. This is consistent with $\tilde{L} \approx 0.2$ at the superheat limit of many real materials[2]; it is comparable to the value 0.18 obtained in colloidal crystals[14] and only slightly smaller than the value 0.22 for the Lennard-Jones system[28].

4 Conclusions

The nature of instability at the superheat limit is related to the fundamental mechanism of crystal melting[2], but it is difficult to measure because crystals are unstable close to the limit and there is a lack of theoretical guidance on how to perform extrapolation. We propose a physical formula for hard spheres based on a revised version of Speedy's EOS which fits all of the measured elastic moduli and pressure closely (Fig. S6). As a byproduct, our revised EOS shows a better accuracy than previous EOSs of hard-sphere crystals especially at low densities. We identified the superheat limit of a hard-sphere fcc crystal at $\phi_{\text{limit}} = 0.494 \pm 0.003$, where the spinodal lattice instability $B = 0$ preempts all other instabilities, including the conventional Born's shear instability. This mechanical result is not related to the dynamics, thus independent to the simulation methods. The superheat limit can be accurately identified using either the finite-size effect of the MFPT or the generalized equation of state rather than conventional polynomial extrapolations. These two new methods for superheat limit studies can be applied in other experimental or simulation systems.

Before reaching the superheat limit, the homogeneous melting kinetics follows the conventional one-step nucleation without any intermediate state. During such a melting process, the evolutions of various order parameters and pressure exhibit the universal compressed exponential function which has not been observed or explored in other melting systems. The compressed exponential function has an unusually large β, posing a new challenge to melting theory.

Acknowledgment

The authors are grateful for useful discussions with Yang Xiang and Kiwing To. This work was supported by RGC grants GRF16301514 and A-HKUST616/14.

References

1 J. G. Dash, A. W. Rempel and J. S. Wettlaufer, *Rev. Mod. Phys.*, 2006, **78**, 695–741.
2 Q. S. Mei and K. Lu, *Progress in Materials Science*, 2007, **52**, 1175–1262.
3 F. Wang, D. Zhou and Y. Han, *Adv. Funct. Mater.*, 2016, **26**, 8903–8919.
4 E. Wigner, *Phys. Rev.*, 1934, **46**, 1002–1011.
5 F. Krzakala and L. Zdeborová, *J. Chem. Phys.*, 2011, **134**, 034512.
6 F. Krzakala and L. Zdeborová, *J. Chem. Phys.*, 2011, **134**, 034513.
7 A. Okounkov, N. Reshetikhin and C. Vafa, *The Unity of Mathematics*, Birkhäuser Boston, 2006, pp. 597–618.
8 B. Li, F. Wang, D. Zhou, Y. Peng, R. Ni and Y. Han, *Nature*, 2016, **531**, 485–488.
9 A. M. Alsayed, M. F. Islam, J. Zhang, P. J. Collings and A. G. Yodh, *Science*, 2005, **309**, 1207–1210.
10 J. Daeges, H. Gleiter and J. Perepezko, *Phys. Lett. A*, 1986, **119**, 79–82.

View Article Online
DOI: 10.1039/C7SM02291C

11 F. Banhart, E. Hernández and M. Terrones, *Phys. Rev. Lett.*, 2003, **90**, 185502.
12 J. W. Herman and H. E. Elsayed-Ali, *Phys. Rev. Lett.*, 1992, **69**, 1228–1231.
13 B. J. Siwick, J. R. Dwyer, R. E. Jordan and R. J. D. Miller, *Science*, 2003, **302**, 1382–1385.
14 Z. Wang, F. Wang, Y. Peng, Z. Zheng and Y. Han, *Science*, 2012, **338**, 87–90.
15 Z. Wang, F. Wang, Y. Peng and Y. Han, *Nat. Commun.*, 2015, **6**, 6942.
16 R. F. Wood and G. E. Jellison, *Semiconductors and Semimetals*, 1984, **23**, 165–250.
17 V. I. Tarzhanov, *Shock Waves*, 1999, **9**, 307–311.
18 B. I. Halperin and D. R. Nelson, *Phys. Rev. Lett.*, 1978, **41**, 121–124.
19 S. T. Chui, *Phys. Rev. Lett.*, 1982, **48**, 933–935.
20 K. Zahn, R. Lenke and G. Maret, *Phys. Rev. Lett.*, 1999, **82**, 2721–2724.
21 Y. Han, N. Y. Ha, A. M. Alsayed and A. G. Yodh, *Phys. Rev. E*, 2008, **77**, 041406.
22 E. P. Bernard and W. Krauth, *Phys. Rev. Lett.*, 2011, **107**, 155704.
23 S. C. Kapfer and W. Krauth, *Phys. Rev. Lett.*, 2015, **114**, 035702.
24 M. Zu, J. Liu, H. Tong and N. Xu, *Phys. Rev. Lett.*, 2016, **117**, 085702.
25 R. W. Cahn, *Nature*, 1986, **323**, 668–669.
26 R. W. Cahn, *Nature*, 1988, **334**, 17–18.
27 H. J. Fecht and W. L. Johnson, *Nature*, 1988, **334**, 50–51.
28 Z. H. Jin, P. Gumbsch, K. Lu and E. Ma, *Phys. Rev. Lett.*, 2001, **87**, 055703.
29 R. W. Cahn, *Nature*, 2001, **413**, 582–583.
30 M. Forsblom and G. Grimvall, *Nat Mater*, 2005, **4**, 388–390.
31 A. Samanta, M. E. Tuckerman, T.-Q. Yu and W. E, *Science*, 2014, **346**, 729–732.
32 M. Isobe and W. Krauth, *J. Chem. Phys.*, 2015, **143**, 084509.
33 A. Isihara, *Condensed Matter Physics*, Courier Corporation, 2014.
34 P. N. Pusey and W. van Megen, *Nature*, 1986, **320**, 340–342.
35 *Theory and Simulation of Hard-Sphere Fluids and Related Systems*, ed. A. Mulero, Springer, Berlin, 2008.
36 W. G. Hoover and F. H. Ree, *J. Chem. Phys.*, 1968, **49**, 3609–3617.
37 H. Xu and M. Baus, *Phys. Rev. A*, 1988, **38**, 4348–4350.
38 J. F. Lutsko and M. Baus, *Phys. Rev. Lett.*, 1990, **64**, 761–763.
39 C. F. Tejero, M. S. Ripoll and A. Pérez, *Phys. Rev. E*, 1995, **52**, 3632–3636.
40 A. R. Denton, N. W. Ashcroft and W. A. Curtin, *Phys. Rev. E*, 1995, **51**, 65–73.
41 C. P. Royall, W. C. Poon and E. R. Weeks, *Soft Matter*, 2013, **9**, 17–27.
42 P. J. Steinhardt, D. R. Nelson and M. Ronchetti, *Phys. Rev. B*, 1983, **28**, 784–805.
43 P.-R. ten Wolde, M. J. Ruiz-Montero and D. Frenkel, *Faraday Discuss.*, 1996, **104**, 93.
44 W. Lechner and C. Dellago, *J. Chem. Phys.*, 2008, **129**, 114707.
45 S. Alexander and J. McTague, *Phys. Rev. Lett.*, 1978, **41**, 702–705.
46 U. Gasser, E. R. Weeks, A. Schofield, P. N. Pusey and D. A. Weitz, *Science*, 2001, **292**, 258–262.
47 T. Kawasaki and H. Tanaka, *PNAS*, 2010, **107**, 14036–14041.
48 W. Qi, Y. Peng, Y. Han, R. K. Bowles and M. Dijkstra, *Phys. Rev. Lett.*, 2015, **115**, 185701.
49 P. Tan, N. Xu and L. Xu, *Nat. Phys.*, 2014, **10**, 73–79.
50 C. F. Tejero and J. A. Cuesta, *Phys. Rev. E*, 1993, **47**, 490–495.
51 J. C. Phillips, *Rep. Prog. Phys.*, 1996, **59**, 1133.
52 P. G. Debenedetti, *Metastable Liquids: Concepts and Principles*, Princeton University Press, Princeton, N.J, 1996.
53 M. Leitner, B. Sepiol, L.-M. Stadler and B. Pfau, *Phys. Rev. B*, 2012, **86**, 064202.
54 L. Cipelletti, S. Manley, R. C. Ball and D. A. Weitz, *Phys. Rev. Lett.*, 2000, **84**, 2275–2278.
55 P. Falus, M. A. Borthwick, S. Narayanan, A. R. Sandy and S. G. J. Mochrie, *Phys. Rev. Lett.*, 2006, **97**, 066102.
56 P. Ballesta, A. Duri and L. Cipelletti, *Nat. Phys.*, 2008, **4**, 550–554.
57 T. Morishita, *J. Chem. Phys.*, 2012, **137**, 024510.
58 B. Ruta, G. Baldi, G. Monaco and Y. Chushkin, *J. Chem. Phys.*, 2013, **138**, 054508.
59 C. Caronna, Y. Chushkin, A. Madsen and A. Cupane, *Phys. Rev. Lett.*, 2008, **100**, 055702.
60 G. Grimvall, B. Magyari-Köpe, V. Ozoliņš and K. A. Persson, *Rev. Mod. Phys.*, 2012, **84**, 945–986.
61 L. B. Pártay, A. P. Bartók and G. Csányi, *Phys. Rev. E*, 2014, **89**, 022302.
62 D. Frenkel and A. J. C. Ladd, *Phys. Rev. Lett.*, 1987, **59**, 1169–1169.
63 J. Wang, J. Li, S. Yip, S. Phillpot and D. Wolf, *Phys. Rev. B*, 1995, **52**, 12627–12635.
64 R. J. Speedy, *J. Phys. Condens. Matter*, 1998, **10**, 4387–4391.
65 O. Farago and Y. Kantor, *Phys. Rev. E*, 2000, **61**, 2478–2489.
66 K. Huang, *Introduction to statistical physics*, Taylor & Francis, London; New York, 2001.

View Article Online
DOI: 10.1039/C7SM02291C

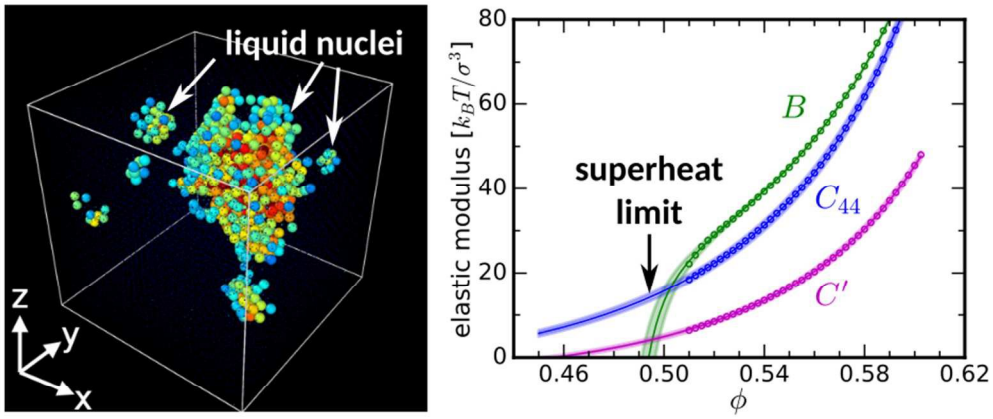

333x166mm (72 x 72 DPI)